



## Crushing behavior of contact-aided AlSi10Mg sandwich structure based on chiral mechanical metamaterials

Weiyun Xu<sup>a</sup>, Lei Zhang<sup>a</sup>, Boqin Zhang<sup>a</sup>, Hanyu Zhang<sup>a,\*</sup>, Zhao Liu<sup>b,\*</sup>, Ping Zhu<sup>a,\*</sup>

<sup>a</sup> The State Key Laboratory of Mechanical System and Vibration, National Engineering Research Center of Automotive Power and Intelligent Control, School of Mechanical Engineering, Shanghai Jiao Tong University, Shanghai, China

<sup>b</sup> School of Design, Shanghai Jiao Tong University, Shanghai, China



### ARTICLE INFO

#### Keywords:

Chiral mechanical metamaterials  
twist effect  
crushing behavior  
contact  
sandwich structure  
energy absorption

### ABSTRACT

With additional rotation degrees of freedom, chiral mechanical metamaterials reveal a prospect in impact resistance and energy absorption by both facilitating the bending-dominated characteristics in deformation and enabling possible energy dissipation through contact among unit cells. However, the corresponding structure-property relationships are still understudied considering more complex deformation modes. In this paper, the impact of the compression-to-twist effect of chiral metamaterials on the crushing behavior was systematically investigated. We proposed a design framework of chiral metamaterials enabling the intercellular contact during twisting deformation. Through the manufacture, simulation, and experiment of AlSi10Mg sandwich structures composed of chiral metamaterials, the multi-segment mechanical response of the designed sandwich core to a crush load was demonstrated and discussed. Moreover, the unique deformation and failure mechanism was embodied in the derived specific energy absorption (SEA) and compressive modulus. The proposed metamaterial with a contact-aided twist is light-weight and high in SEA, elucidating a practical way of combining bending-dominated and stretching-dominated lattices. It paves the road for designing metamaterials with graded energy absorption performance, rigid-flexible coupling properties, multi-functional responses, etc.

### 1. Introduction

Mechanical metamaterials with extraordinary mechanical performances and light-weight properties are widely used in fields of energy-absorbing, buffering, and shock absorption [1–4]. Their performance can even exceed that of nature materials by rationally designing the microstructure and macro configuration, including negative Poisson's ratio [5], programmable elasticity [6], multi-stability [7,8], improved damage tolerance [9], etc. Recently, mechanical metamaterials with structural chirality namely chiral mechanical metamaterials have undergone extensive research interests [10,11]. "Chiral" refers to the symmetry-breaking property of the material's microstructure. With additional rotation degrees of freedom (DOF) that no longer satisfies the classic Cauchy continuum theory, chiral mechanical metamaterials exhibit unique chiral effects, i.e., twists upon pulling or pushing, which has been studied and applied in soft robots [12], compliant mechanisms [13], acoustics and vibration [14,15], etc. Meanwhile, chiral mechanical metamaterials are ideal for energy absorbing with regard to the bending-dominated characteristics of deformation, which contains

elastic buckling, plastic bending, and fracturing of the microstructure [16].

Concerning the energy-absorbing capability, efforts have been made to obtain large twist of chiral metamaterials and investigate the possible mechanism. T. Frenzel et al. proposed 3D chiral elastic metamaterials with twists per axial strain exceeding 2°/% [11] and later improved the sample-size dependence of the rotation property by connecting unit cells with compliant structures [17]. As a typical chiral configuration, unit cells with Z-shaped diagonal rods were analyzed using an instant pseudo-rigid-body model (PRBM) by W. Xu et al. [18] to investigate the underlying deformation mechanism. Results showed that the compress-to-twist coupling is sensitive to the geometry parameters. L. Meng et al. [19] tested the load-bearing capacity using resin sandwich plate arranged by hyperbolic cellular materials with twist effects. Through unidirectional compression and drop-impact test, it showed that the large rotational deformations of the chiral unit cells are advantageous to the design of buffering plates or energy-absorbing devices. Meanwhile, the twist behavior embodied in tensegrity architecture proposed by Z. Vangelatos et al. [20] revealed an

\* Corresponding authors.

E-mail addresses: [zhanghanyu@sjtu.edu.cn](mailto:zhanghanyu@sjtu.edu.cn) (H. Zhang), [hotlz@sjtu.edu.cn](mailto:hotlz@sjtu.edu.cn) (Z. Liu), [pzhu@sjtu.edu.cn](mailto:pzhu@sjtu.edu.cn) (P. Zhu).

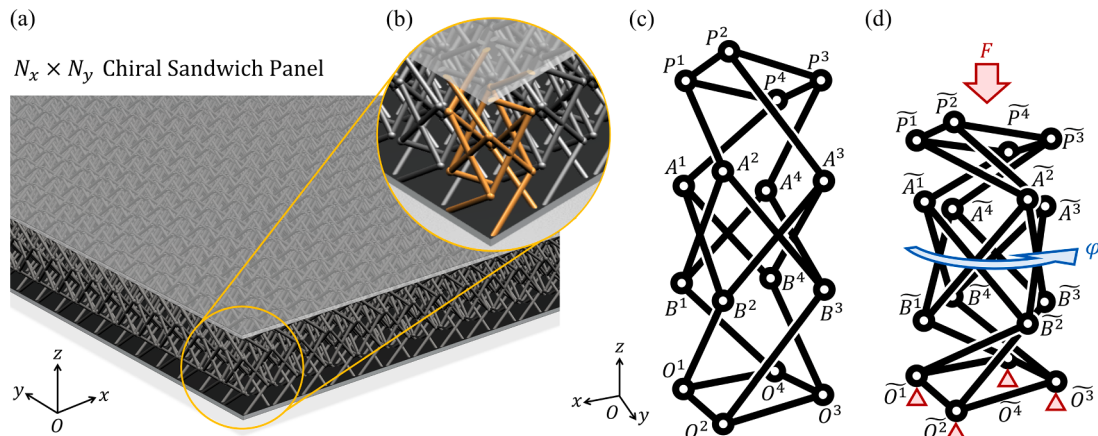


**Fig. 1.** The proposed sandwich panel based on chiral mechanical metamaterials. (a) The sandwich panel whose core layer is based on  $N_x \times N_y$  (b) chiral unit cells. (c) The characterization of the proposed chiral unit cell in (b) by instant pseudo-rigid-body model (PRBM) and (d) the rotation response (angle  $\varphi$ ) under the uniaxial compression  $F$  with  $\widetilde{O}^i$  fixed. The positions of joints before and after deformation are denoted as  $X^i$  and  $\widetilde{X}^i$  respectively ( $X = A, B, P, O$ ;  $i = 1, 2, 3, 4$ ).

alternative way to integrate chirality with buckling. Furthermore, different chiral and anti-chiral tessellations utilizing negative Poisson's ratio have been investigated [5,21] which exhibit good performance in energy absorption, but the designs are restricted to either two-dimensional (2D) structures or planar-patterns-based tubes.

Ulteriorly, some results have demonstrated that chiral metamaterials are relatively more compliant than conventional lattices, e.g., BCC lattice [22,23], Kagome [24]. It was also reported that the stiffness of metamaterials was reduced to gain high chiral effects [18]. Essentially, this complicated deformation mode enables possible potential for energy absorber composed of chiral metamaterials in compression resistance and adaptable mechanical response. On the one hand, it was demonstrated that the coupled rotation deformation under axial load leads to formation of more plastic hinges, benefiting the conversion from external work to the elastic and plastic energy of materials [19]. The contact of microstructures during large deformation, on the other hand, could change the initial stiffness of chiral metamaterials and increase the dissipated energy [25], causing sudden mode changes in mechanical behavior. For structures with chiral unit cells tessellation, the contact under compression could be a key characteristic that enables unique deformation pattern and good energy absorption performance. While most of current research relies on the contact within unit cell by either densifying the gap between diagonal bars [19] or rationally generating microstructures that introduce surface contact [25,26], few research pays attention to the intercellular contact.

This study aims to reveal the deformation mechanism and failure mode contributing to the design for energy absorption of chiral mechanical metamaterials. Creatively, we raise the interest in the contact behavior between chiral unit cells, try to design the chiral geometry with a new perspective, and explore the underlying deformation mechanism. Therefore, in Section 2, we proposed a heuristic design method of metamaterials with contact-aided twist behavior, which was applied to sandwich structures composed of contacted chiral metamaterials (CCM) and non-contacted chiral metamaterials (NCM). The contact was controlled by parametric model considering additive manufacturing (AM), along with a rigorous derivation of the relative density of the metamaterial to obtain specific energy absorption (SEA). Next in Section 3, selective laser melting (SLM) AlSi10Mg samples of chiral sandwich panels with/without contact-aided cores were fabricated, tested, and simulated in order to analyze the deformation mechanism and failure mode of the crushing behaviors. The corresponding SEA, specific compressive modulus, and densification strain were derived on the basis of the stress-strain curves. Based on the insights from mechanical tests, the relationship between the energy-absorbing capabilities and the design space was validated by finite element analysis (FEA). In the end,

the article concludes with a summary of this work in Section 4, pointing out limitations and possible future applications.

## 2. Materials and method

In this section, we first demonstrated the proposed design framework of CCM/NCM sandwich panels, where a parametric model was derived. We then presented the manufacturing process of the sandwich samples along with the experimental method. Following that, the corresponding finite element analysis (FEA) was introduced.

### 2.1. Design of sandwich core layer with contact-aided twist

#### 2.1.1. Design and modeling of CCM/NCM unit cell

A typical sandwich structure consists of a core layer and the upper and lower panels and absorbs energy mainly depending on the plastic deformation of the core layer. Herein, we mainly designed the core layer by periodic filling with chiral metamaterial unit cells. To improve the potential energy absorption performance of the sandwich structure using contact, the chiral metamaterial unit cell should possess a significant compression-to-rotation deformation of mechanical response. And geometrically, both a certain area for the contact after rotation and a proper distance between adjacent unit cells should be satisfied. Considering these conditions and the convenience of manufacturing, we choose one of the most representative categories of chiral unit cells – Z-shaped architecture which contains multiple diagonal rods around one specific axis [27] – to generate a periodic configuration. Composed of strut-based structures with Z-shaped motif, the Z-shaped chiral unit cell shows a good compression-to-twist performance and embodies in various types of chiral metamaterials [28]. It is worth pointing out that, the proposed design frame work could also be general by replace the Z-shaped unit cell by other chiral microstructures.

As shown in Fig. 1(a), the core layer contains  $N_x$  and  $N_y$  numbers of unit cells in  $x$  and  $y$  directions respectively, denoted as  $N_x \times N_y$ . There is only one layer of unit cells along  $z$ -axis, because the intercellular contact behavior is designed to happen perpendicular to the load direction ( $xOy$  plane), and the twist is only linear superposition with the number of cells in  $z$  direction. Next, along  $z$ -axis within each unit cell, two Z-shaped chiral structures with opposite handedness were piled so that their respective rotations will combine in the middle of the unit cell but cancel each other at the two ends, which avoids additional constraint torsions on the upper and lower panels. The left-handedness above and right-handedness below were applied, as demonstrated in Fig. 1(c) and (d). We named these chiral structures in the sandwich core layer the chiral parts for convenience, as shown in Fig. 2(a). Furthermore, inspired by

**Table 1**

Independent parameters of representative chiral mechanical metamaterials.

$L_1$ (mm)	$h_c$ (mm)	$a_1/L_1$	$a_2/h_c$	$b/L_1$	$d$ (mm)	$d'$ (mm)	Denotation
8	18	0.8	0.4	0.9	0.7	1.0	CCM-F-8
8		0.8	0.0				CCM-T-8
8		0.4	0.4				NCM-F-8
8		0.4	0.0				NCM-T-8
10		0.8	0.4				CCM-F-10
10		0.8	0.0				CCM-T-10

Thickness of the upper and lower sheets  $t_1 = t_2 = 1$  mm.

our previous design [18], a cubic space was employed between the two chiral parts to ensure a contact area, namely the achiral part. Considering the design constraints for 3D-printing self-supported structure, the achiral part was constructed using inclined rods, which made it a face-centred-cubic-like topology (represented as FCC in this paper).

To facilitate the analysis of the deformation, we described the behavior of the unit cell using an instant pseudo-rigid-body model (PRBM) [29,30] which models flexible components as rigid segments connected by revolute joints and ignored the local deformation within each component, as shown in Fig. 1(c). The deformation trend (Fig. 1d) reveals that the uniaxial compressive displacement on top made the achiral part ( $\tilde{A}^i$  and  $\tilde{B}^i$ ,  $i = 1, 2, 3, 4$ ) rotate while remaining the top and the bottom ( $\tilde{P}^i$  and  $\tilde{O}^i$ ,  $i = 1, 2, 3, 4$ ) irrotational. And  $\tilde{A}^i$  and  $\tilde{B}^i$  would approach  $\tilde{P}^i$  and  $\tilde{O}^i$  respectively as the load along z-axis continues, indicating the possibility for the achiral part to contact with the upper and lower panels. Therefore, the “chiral part + achiral part + chiral part” unit-cell design framework enables sandwich structures with a flexible design space utilizing the additional rotation DOF of chiral metamaterial. Following the proposed design method, the contact behaviour can be introduced during the compressive deformation of sandwich core layers.

### 2.1.2. Parametric design of CCM/NCM sandwich structure

In this work, we investigated the structure-property (S-P) relationships of the proposed chiral metamaterial by parameterization. As shown in Fig. 2(a), with a size of  $L_1 \times L_1 \times h_c$ , the chiral unit cell is composed of rod components and joints that connect these rods. The length of the rod components in the chiral parts is  $l_1$ , the length of the rods in the achiral part is  $l_2$ , and the thickness of the upper and the lower panels is  $t_1 = t_2 = t$ . We defined three types of joints according to their positions and geometries: Joint 1 connects the inclined rods in achiral part, Joint 2 connects the chiral and achiral parts, and Joint 3 connects the chiral parts and the panels. Herein, all rods were assigned to uniform circular section with diameter  $d$  and Joint 2 were spherical with diameter  $d'$  bigger than  $d$ . Thus, the S-P relationship can be expressed by independent geometrical parameters as

$$\mathbf{P} = \mathbf{S}(a_1, a_2, b, d, d', L_1, h_c, t), \quad (1)$$

and the other parameters can be derived by these parameters as

$$\begin{aligned} \Delta h &= \frac{t}{2}, \\ l_1 &= \frac{1}{2} \sqrt{(b + a_1)^2 + (b - a_1)^2 + (h_c + 2\Delta h - a_2)^2}, \\ l_2 &= \sqrt{a_1^2 + a_2^2}, \\ \tan \alpha &= \frac{h_c + 2\Delta h - a_2}{b + a_1}, 0 < \alpha < \frac{\pi}{2}, \\ \tan \beta &= \frac{h_c + 2\Delta h - a_2}{b - a_1}, 0 < \beta < \pi, \\ \tan \frac{\theta}{2} &= \frac{a_1}{a_2}, 0 < \theta < \pi. \end{aligned} \quad (2)$$

It is noted that stress concentrations in lattice-type materials due to

the microstructural characteristics are inevitable, mainly embodied in the increases of localized stress that is caused by abrupt cross-sectional changes and surface discontinuities at the joints between rod structures. Although some studies have been conducted to improve the stress concentration and the corresponding mechanical properties by designing reinforcement nodes with gradual cross-sectional changes [23], the aim of this paper is to investigate the special deformation patterns underlying chiral metamaterials. Thus, we choose to preserve the most primitive geometrical features of rods and joints.

Referring to Fig. 2(a), various categories of unit cells can be generated by controlling the ratio of the length of the achiral part to the length of the unit cell  $a_1/L_1$ , and the ratio of the height of the achiral part to the height of the unit cell  $a_2/h_c$ . Apparently, we have  $a_1/L_1 \in (0, 1)$  and  $a_2/h_c \in (0, 1)$ . Moreover, by the insights from the PRBM and the analysis of two-unit-cells model as shown in Fig. 2(e), we can determine whether a contact behavior happens between unit cells using a boundary of design domain defined as

$$\mathbf{f}(a_1, a_2, b, d, L_1, h_c) = 0, \quad (3)$$

and thus derive the design domain of contacted chiral metamaterials (CCM) by

$$\begin{aligned} 2l_1^2 &> a_1^2 + \sqrt{2}a_1b + b^2, \\ \sqrt{2} \frac{a_1}{L_1} + \frac{d}{L_1} &> 1. \end{aligned} \quad (4)$$

Conversely, designs that don't meet the criteria in Eq. (4) are denoted as non-contacted chiral metamaterials (NCM). Interestingly, through our generalized parameterization of chiral metamaterials, the FCC lattice of the achiral part transforms into a square as the ratio  $a_2/h_c$  turns to zero, causing the topology of the unit cell to change into the normal Z-shaped one. Thus, this generalized parametric design enables us to include representative unit cell types by varying  $a_1/L_1$  and  $a_2/h_c$ , as shown in Table 1 and Fig. 3.

### 2.1.3. Relative density of CCM/NCM

As one of the dominant factors of the value of specific energy absorption (SEA), the relative density is an important indicator for energy absorbing materials. In general, the relative density of architected material can be calculated from the ratio of the actual volume of the material to the volume of space it occupies, as  $\rho^*/\rho_s = V_m/V_s$ . With  $\rho_s = 2.68 \text{ g/cm}^3$  for AlSi10Mg and  $V_s = L_1^2 h_c$ , the challenge in obtaining  $V_m$  of the chiral unit cell in this study, however, lies in the calculation of the volume of the joints. A simplified way is to multiply the sum of the line lengths of all rod components by the cross-sectional area, ignoring how the rods are connected and the overlapping volumes caused by it. Small the effect may appear to be, results below (Table 2) show that this makes a significant difference to an accurate calculation, especially when the rods are thick. We have therefore derived an analytical expression for the relative density by rigorously calculating the overlapping volume between the rods and joints. Specifically, we obtained the volumes of three different joints (Fig. 2, b to d), expressed as

$$\begin{aligned} V_{j1} &= \iint \sqrt{\frac{d^2}{4} - r^2} r dr d\theta = \frac{\pi d^3}{12} \left[ \lambda^3 - (\lambda^2 - 1)^{\frac{3}{2}} \right], \lambda = \frac{d}{d'}, \lambda \geq 1, \\ V_{j2} &= \frac{2d^3}{3 \sin \theta}, 0 < \theta < \pi, \\ V_{j3} &= \frac{\pi d^2 \Delta h \sqrt{\tan^2 \alpha + \tan^2 \beta + \tan^2 \alpha \tan^2 \beta}}{4 \tan \alpha \tan \beta}. \end{aligned} \quad (5)$$

Then the relative density can be expressed by geometrical parameters as

$$\frac{\rho^*}{\rho_s} = \frac{V_m}{V_s} = \frac{8l_1 s + 8l_2 s + 8V_s - 24V_{j1} - 4V_{j2} - 8V_{j3}}{L_1^2 h_c} \times 100\%, \quad (6)$$

**Table 2**

Relative density of the proposed chiral sandwich core layer.

Unit cell types	Analytical		Simplified analytical		Experimental		CAD
	$\rho^*/\rho_s(\%)$	$err_{rel}(\%)$	$\rho^*/\rho_s(\%)$	$err_{rel}(\%)$	$\rho^*/\rho_s(\%)$	$err_{rel}(\%)$	$\rho^*/\rho_s(\%)$
CCM-F-8	4.80	0.25	5.08	6.04	4.91	2.44	4.79
CCM-T-8	3.77	0.28	3.98	5.98	3.87	2.95	3.76
NCM-F-8	4.11	1.46	4.40	8.59	4.31	6.50	4.05
NCM-T-8	3.17	0.15	3.37	6.62	3.23	2.08	3.16
CCM-F-10	3.47	0.14	3.67	5.84	3.72	7.34	3.47
CCM-T-10	2.72	0.39	2.87	5.79	2.75	1.43	2.71

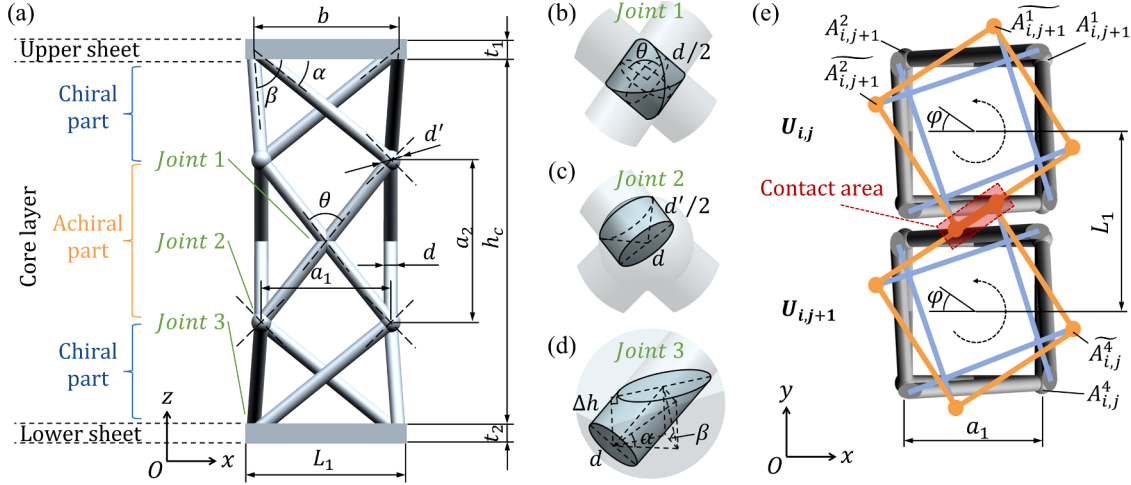


**Fig. 2.** The parametrical design of the chiral sandwich structure. (a) The parameterized chiral unit cell of the proposed sandwich panel. The overlapping volumes of rod components by Joint 1, Joint 2, and Joint 3 are shown in (b), (c), and (d) respectively. (e) Top view of the two-unit-cells model, where the achiral parts rotate through angle  $\varphi$  and encounter with each other within the contact area.  $U_{i,j}$  and  $U_{i,j+1}$  refer to the two unit cells along y-axis, and  $A_{i,j}^m$  ( $\widehat{A}_{i,j}^m$ ,  $m = 1, 2, 3, 4$ ) denotes Joint 2 of four vertices before (after) rotation.

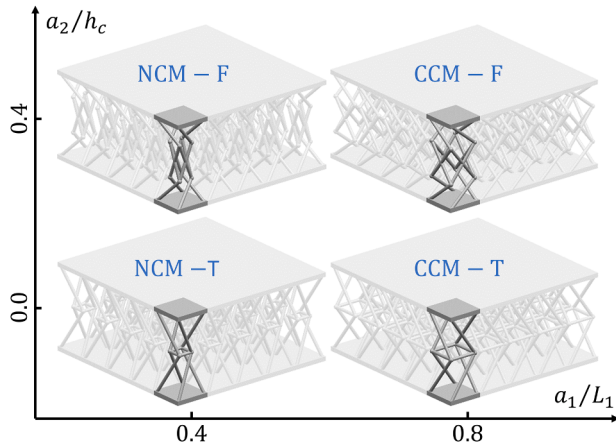


**Fig. 3.** Parametric design of the proposed CCM/NCM sandwich structures. Four representative types are determined by  $(a_1/L_1, a_2/h_c) = (0.4, 0), (0.4, 0.4), (0.8, 0)$ , and  $(0.8, 0.4)$  in the coordinate. “CCM-F-8” refers to the sandwich core layer based on contacted chiral metamaterials of 8mm-long-unit-cell with face-centred cubic as the achiral part and “CCM-T-8” refers to that with the typical unit cell in literature [27,28], and so on to the other abbreviations.

**Table 3**  
Process parameters set up of SLM.

Parameter	Value
Laser thickness ( $\mu\text{m}$ )	30
Hatch distance ( $\mu\text{m}$ )	80
Laser speed (mm/s)	1600
Laser power (W)	370
Beam offset ( $\mu\text{m}$ )	20
Stripe width (mm)	5
Overlap ( $\mu\text{m}$ )	50

where

$$S = \frac{\pi d^2}{4}, \quad (7)$$

$$V_s = \frac{\pi \lambda^3 d^3}{6}.$$

The results by the analytical expression were compared with the afore-mentioned simplified method, the actual measured values of fabricated samples (experimental), and the values directly from the CAD software, as shown in Table 2. Taking the values of CAD software as reference, the table also shows the relative error of each method.

With the geometrical parameters set as Fig. 3, the relative density of the proposed chiral metamaterials is within 5%. And the relative error of the analytical solution is less than 1.5%, indicating the effectiveness of the analytical solution. It should be pointed out that the analytical solution of the relative density will be used for the subsequent numerical study of the S-P relationships, and the experimental values will be used to directly calculate the SEA of these physical samples.

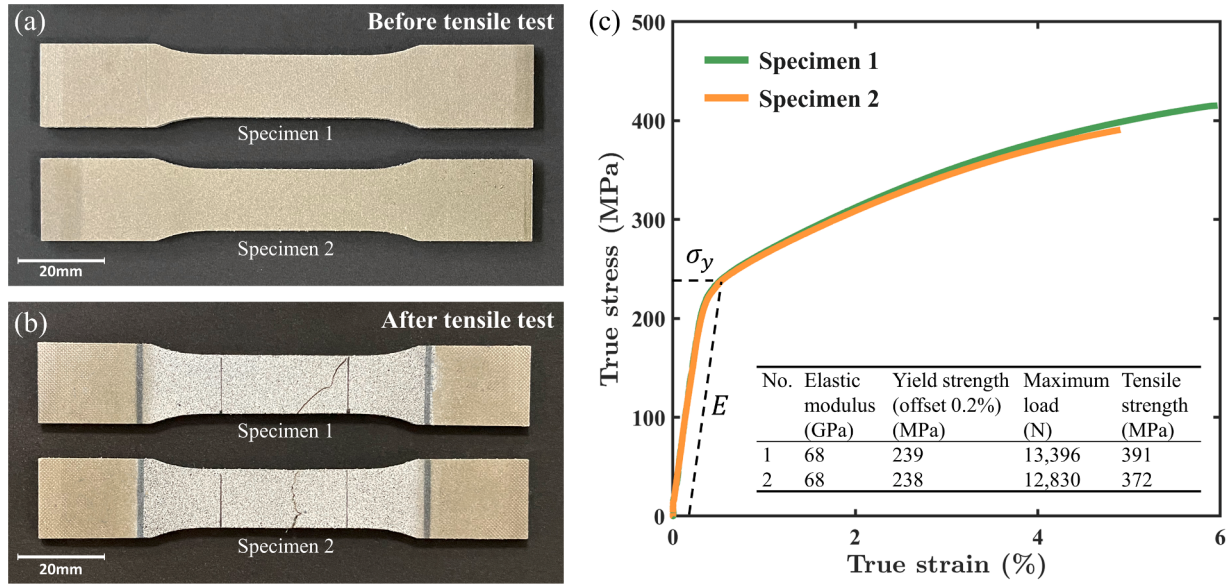


**Fig. 4.** Result of tensile test of the SLM AlSi10Mg specimens. 3D-printed AlSi10Mg specimens (a) before and (b) after tensile test with DIC spraying. (c) Stress-strain curves of the specimens. Both representative ductile and brittle fracture types were presented. Tensile rate: 0.04mm/s.

## 2.2. Fabrication and flatwise compression of CCM/NCM sandwich structures

Referring to Fig. 3, sandwich samples with the four categories of chiral core layers were fabricated for a further physical experiment to explore their energy absorption properties and underlying mechanisms. With 40mm × 40mm × 20mm of overall size, all sandwich samples were manufactured by selective laser melting (SLM) technique using a 3D Systems DMP 320 metal 3D Printer. Considering the light-weight characteristic and the higher strength and hardness compared to other aluminum alloys, we chose AlSi10Mg as the constituent material. The AM process parameters were technically set according to the process parameter database from the equipment manufacturer, as shown in Table 3. To release thermal stress, all samples were heat-treated in accordance to ASTM F3301-18a to a maximum temperature of 300°C, held constant for 2 hours, and acclimated back to room temperature in the air.

Additionally, we ensured that the manufacturing provided a reliable build quality of the structures through dimensional analysis (refer to Appendix A for details). By measuring the overall height  $h = h_c + 2t$ , the sheet thickness  $t$ , and the strut diameter  $d$  of the fabricated samples, it illustrated that the process parameters and thermal post-processing guaranteed the forming accuracy in geometry.

Referring to ASTM C365-00 for the proposed sandwich samples, flatwise compressive tests were conducted utilizing the electrical universal testing machine Instron 5982. The samples were clamped by a compression fixture with a spherical support. And to guarantee the uniaxial quasi-static compression condition, a compressive load at a strain rate of  $9.26 \times 10^{-4}\text{s}^{-1}$  was imposed vertically on the upper panel until crush. The force-displacement curves were recorded and then processed into stress-strain curves. Meanwhile, the in-situ observation with respect to different deformation stages was recorded by photography equipment. It is noted that, to obtain the mechanical property of AlSi10Mg, tensile specimens were also fabricated and then tested, which is presented and discussed in Section 3.1 and Appendix A.

## 2.3. Finite element analysis of CCM/NCM sandwich structures

Herein, we verified the quasi-static compression of the CCM/NCM sandwich structures by finite element analysis (FEA). The ABAQUS explicit solver was used to simulate the experiments. Of the same size as

the manufactured sandwich samples, the established finite element models were assigned the material parameters derived from the mechanical test results of the constituent material (referring to Section 3.1 and Appendix A for details).

Based on the failure modes of AlSi10Mg that contains brittle and ductile fractures, both the ductile damage and shear damage failure criteria based on equivalent plastic strain were applied as the starting criteria for material damage determination [31]. In this way, the fracture initiates once either of the criteria is satisfied. In order to reduce the mesh dependency, max displacement at failure  $\bar{u}_f^{pl}$  with linear softening was determined to describe the damage evolution of AlSi10Mg as

$$\bar{u}_f^{pl} = \frac{2L}{\sigma_{y0}} \int_{\bar{\varepsilon}_0^{pl}}^{\bar{\varepsilon}_f^{pl}} \sigma_y d\bar{\varepsilon}^{pl}, \quad (8)$$

with characteristic element length  $L$  [31]. Additionally, since the sandwich structures were printed as a whole, i.e., the upper and lower panels and core layer were integrated, the interlayer cracking or delamination damage caused by adhesive bonding was not considered.

To be consistent with the experiment, all FEA models were constrained by a uniaxial displacement along z-axis on the top and fixed on the bottom. The sandwich samples were compressed until the axial strain  $\varepsilon_{zz}$  reached 90% with the upper and lower panels both set to be rigid in simulation. The contact in the compression process must be taken into account, mainly in the form of contact between the rod components, and between the rods and the upper and lower panels. Therefore, a general contact interaction was established for analysis, where a hard contact in normal behavior and a friction coefficient of 0.35 in tangential behavior were defined. It should be noted that, the magnitude and direction of the contact forces are closely related to a series of factors, e.g., the relative position, radius, surface roughness of the contacted rods, whereas we assumed the contact behavior as consistent throughout the sandwich structure to simplify the FEA model. Considering the stress concentrations mentioned in Section 2.1, the models were meshed by a combination of hexahedral elements C3D8R and tetrahedral elements C3D4 with approximate global size of 0.07 mm after the convergence analysis (referring to Appendix B for details). Discretized by an average of over 400 million elements, the simulations were carried out utilizing the explicit solver with target time increment

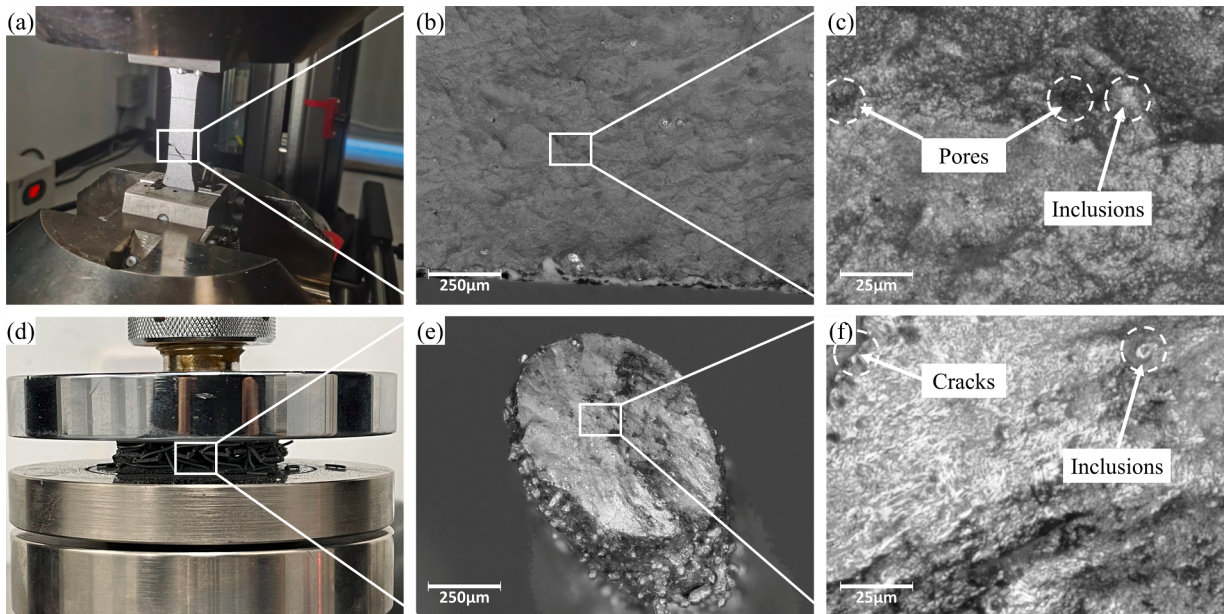


**Fig. 5.** Morphological observation of the SLM specimen and sandwich core layer. (a) Specimen after tensile, and (b) the fracture section view with (c) a magnification of it. (d) The sandwich panel sample in densification stage, and (e) the fracture section view of the corresponding rod component with (f) a magnification of it. The representative defects of materials are marked in (c) and (f).

**Table 4**

Mechanical properties of the proposed chiral sandwich panels in the crush experiment.

Unit cell types	Contact mode	Specific compressive modulus, $E_c$ (MPa·cm <sup>3</sup> /g)	Energy absorption, EA (MJ/m <sup>3</sup> )	Specific energy absorption, SEA (J/g)	End of yield plateau, $\varepsilon_{ple}$ (%)
CCM-F-8	I-II-III	51 (+4.6%)	0.87 (+11.4%)	6.8 (+11.4%)	82.4 (+3.5%)
CCM-T-8	I-II	60 (+17.6%)	0.63 (-0.3%)	6.3 (-0.3%)	82.7 (+2.0%)
NCM-F-8	II-III	75 (+13.4%)	0.74 (+6.2%)	6.7 (+6.4%)	89.5 (-1.0%)
NCM-T-8	II	123 (+2.3%)	0.54 (+4.7%)	6.3 (+4.6%)	81.3 (+1.2%)
CCM-F-10	I-II-III	32 (+8.1%)	0.50 (+4.4%)	5.4 (+4.4%)	87.2 (+3.3%)
CCM-T-10	I-II	40 (+6.0%)	0.25 (+3.6%)	3.5 (+3.5%)	74.5 (+2.7%)

Values in brackets indicate the relative error between the experimental results and the simulation results, where a positive value indicates a larger simulation result.

of  $1 \times 10^{-6}$ .

### 3. Results and Discussion

In this section, we first showed the mechanical properties of the constituent materials and the CCM/NCM sandwich structures. Through in-situ experiment, morphological observations and FEA, the crushing behavior of the CCM/NCM sandwich structure was analysed, and its compressive deformation patterns and failure modes considering contact-aided design were discussed. Following that, the S-P relationships were illustrated. Finally, we demonstrated the effectiveness of the proposed design.

#### 3.1. Mechanical properties of AlSi10Mg CCM/NCM sandwich structures

Through tensile test and compression experiment, the mechanical

properties of AlSi10Mg were tested to define the material properties of the aforementioned FEA, whereas the crush responses of CCM/NCM sandwich structures were obtained as well. As shown in Fig. 4, the uniaxial tensile specimens that were printed together with the sandwich samples fractured at the gauge length sections. And the SLM-fabricated AlSi10Mg exhibited an average elastic modulus of 68GPa and an average elongation at break of 5 ~ 6%, which matched well with the data provided in Table A1.

Thereafter, microscopic observation of the cross-section morphology was carried out through a Keyence digital microscope VHX-7000 in order to further understand the failure mode of the constituent material, as presented in Fig. 5. It can be observed that the fracture sections contain both brittle fractures with a flush section and metallic luster, and slanted ductile fractures at an angle of approximately 45°. We can tell from Fig. 4(c) that the strain at break with brittle fracture is less than that with ductile fracture. Although the selection of constituent material is not the focus of this study and does not affect the main conclusions resulting from the design of metamaterial microstructures, it affects the correct prediction of the simulation results. Based on these results, we can conclude that the SLM AlSi10Mg powder are between brittle and ductile materials, which instructs the finite elements modelling in this work. The fracture mode in the CCM/NCM sandwich samples was consistent with that of the tensile specimens by comparing Fig. 5(c) and (f), where the inclusions and porosity in current 3D printing process were the main manufacturing defects that caused the crack to sprout, expand, and eventually led to damage. Nevertheless, it should be noted that the constitutive model of AlSi10Mg constructed in this study has taken the manufacturing defects into account due to the uniform process parameters.

Meanwhile, the properties of the sandwich samples were measured and calculated. Firstly, the flatwise specific compressive modulus can be determined as:

$$E_c = \frac{\Delta P h_c}{25 \Delta H L_1^2 \rho^*} [\text{MPa} \cdot \text{cm}^3 / \text{g}], \quad (9)$$

where  $\Delta P$  and  $\Delta H$  are the load increment and the corresponding deformation increment of the linear part on the force-displacement curve  $F - s$ . Next, we obtained the energy absorption (EA) by calculating

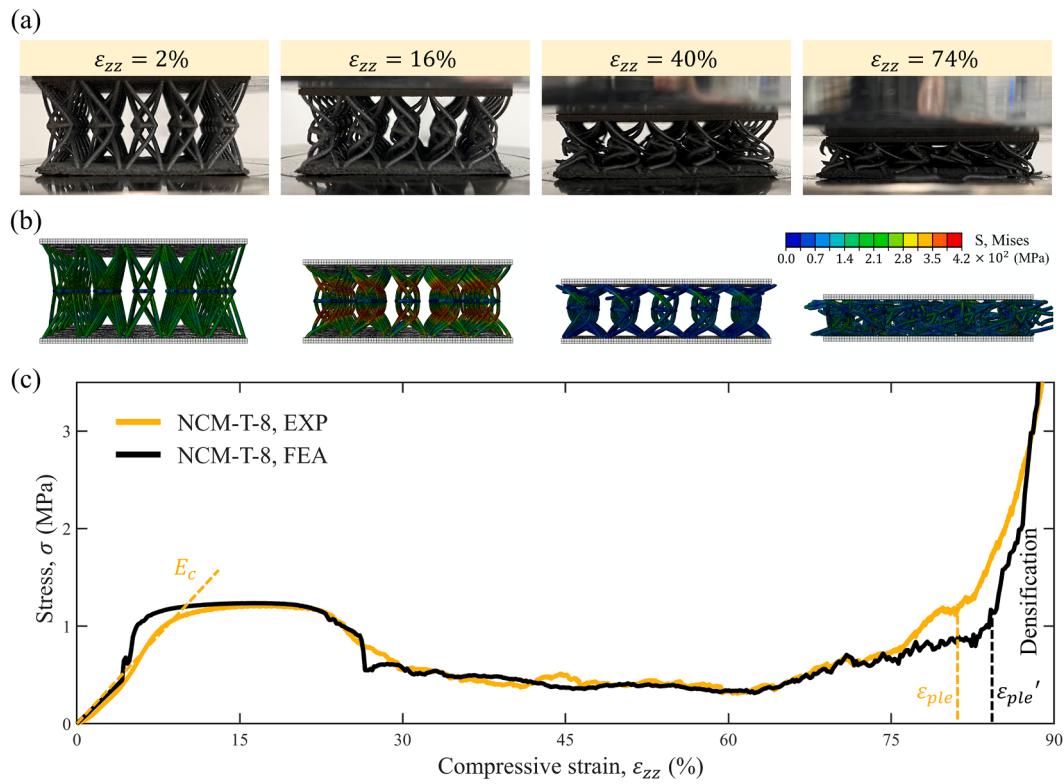


**Fig. 6.** The crushing behavior of NCM-T-8 sandwich structure. (a) In-situ observation of the compressive test at uniaxial strain  $\varepsilon_{zz} = 2\%$ ,  $16\%$ ,  $40\%$ , and  $74\%$  respectively (subfigures from the left to right), and (b) the corresponding FEA deformation history of the compressive procedure. (c) The experimental and numerical stress-strain curves of NCM-T-8. The sandwich sample was printed using SLM with  $5 \times 5 \times 1$  unit cells.

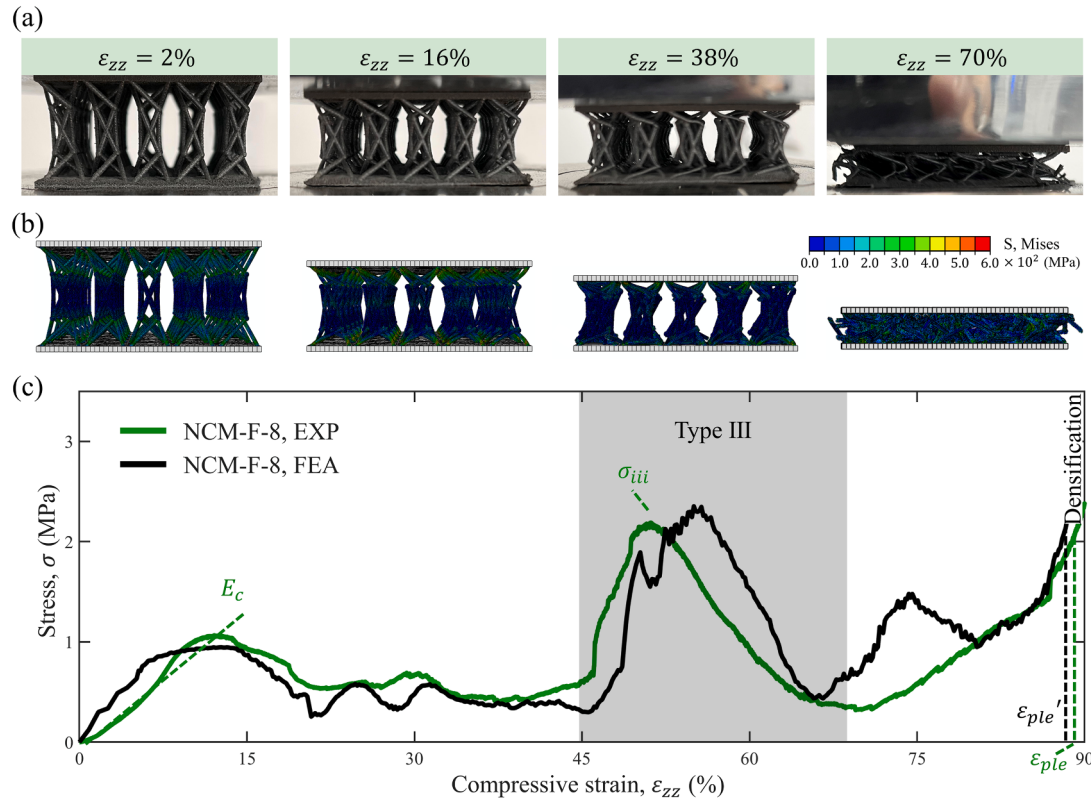


**Fig. 7.** The crushing behavior of NCM-F-8 sandwich structure. (a) In-situ observation of the compressive test at uniaxial strain  $\varepsilon_{zz} = 2\%$ ,  $16\%$ ,  $38\%$ , and  $70\%$  respectively (subfigures from the left to right), and (b) the corresponding FEA deformation history of the compressive procedure. (c) The experimental and numerical stress-strain curves of NCM-F-8. The sandwich sample was printed using SLM with  $5 \times 5 \times 1$  unit cells.

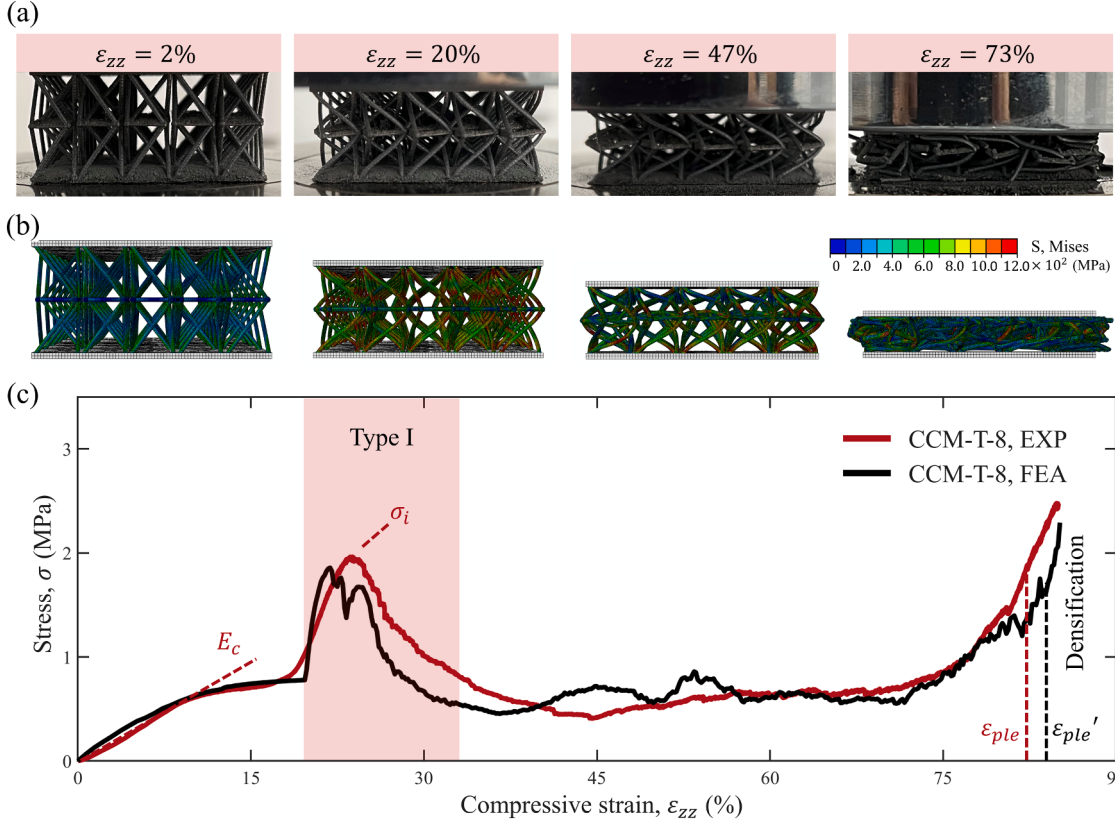


**Fig. 8.** The crushing behavior of CCM-T-8 sandwich structure. (a) In-situ observation of the compressive test at uniaxial strain  $\varepsilon_{zz} = 2\%$ ,  $20\%$ ,  $47\%$ , and  $73\%$  respectively (subfigures from the left to right), and (b) the corresponding FEA deformation history of the compressive procedure. (c) The experimental and numerical stress-strain curves of CCM-T-8. The sandwich sample was printed using SLM with  $5 \times 5 \times 1$  unit cells.

$$EA = \frac{1}{100} \int_0^{\varepsilon_{ple}} \sigma de [\text{MJ / m}^3], \quad (10)$$

where  $\varepsilon_{ple}$  is the plateau end. For an accurate calculation, we defined  $\varepsilon_{ple}$  as the strain corresponding to the maximum deformation efficiency  $f_{max}$  [32] expressed as following:

$$f_{max} = \max \left( \frac{\int_0^s F(s) ds}{F_{max}} \right) - \frac{\int_0^{s_i} F(s) ds}{F_{max}}, \quad s_i \in (0, h_c), \quad (11)$$

$$\varepsilon_{ple} = \frac{l_{max}}{h_c},$$

where  $F_{max} = \max(F|_{0 < s \leq s_i})$  is the maximum force during integration. Therefore, the specific energy absorption (SEA) can be then derived by Eq. (6) and Eq. (10) as:

$$SEA = \frac{EA}{\rho^*} = \frac{\int_0^{\varepsilon_{ple}} \sigma de}{100 \cdot \rho_s \cdot \rho^*/\rho_s} [\text{J / g}]. \quad (12)$$

The results of  $E_c$ , EA, SEA, and  $\varepsilon_{ple}$  are listed in Table 4, and the corresponding crush deformation and energy-absorbing mechanism with respect to the introduced contact behaviors will be discussed in Section 3.2.

### 3.2. Crush behaviors of CCM/NCM sandwich structures

In this study, we conducted the quasi-static crush tests and in-situ observation on the CCM/NCM sandwich structures, and then simulated the crush compression process by finite element analysis (FEA). The stress-strain curves obtained through experiment and simulation match well with each other, as shown in Fig. 6, Fig. 7, Fig. 8, and Fig. 9.

As illustrated in Section 3.1, AlSi10Mg, which is commonly used for casting with a high specific stiffness, is not high in elongation at break compared to many plastic materials (steel, copper, etc.). Although it is usually considered unsuitable for use as a large deformation or plastic material, the 18-millimeters-high sandwich core layer composed by AlSi10Mg continued to carry loads until densification after a uniaxial displacement more than 13mm. Referring to these stress-strain curves, the chiral sandwich panels (mainly the core layer) quickly entered the plastic stage from the elastic stage without an obvious peak stress and maintained a long yield plateau before entering the densification stage at the end of plateau  $\varepsilon_{ple} = 75\% \sim 90\%$ . Nevertheless, the behavior of CCM and NCM at the yield plateau differs with multi-stages depending on whether there is intercellular contact. This indicates a unique property and compressive behavior determined mainly by the designed structure of the chiral metamaterials.

As for the deformation patterns of the proposed CCM and NCM, the deformation history of the CCM/NCM sandwich core layer conformed to the trend of the previously PRBM model analysis. As with all lattice materials, the way the core enters plasticity is to form plastic hinges near the joints, where the stress increases locally until failure occurs. This is a structural characteristic of stress concentration in lattice materials, whereas this deformation pattern is also a way for bending-dominated materials to dissipate energy through plastic deformation. For designs with FCC lattice as the achiral part (CCM-F and NCM-F), the chiral parts always undergo plastic deformation earlier than the achiral part, which implies the relative lower stiffness of chiral metamaterials. As the chiral part deforms, the rotation DOF is reflected driving the achiral part to rotate in the desired direction.

Shared with the aforementioned deformation pattern, the chiral sandwich structure exhibited different responses to uniaxial compression with respect to the unit cell types. First of all, the unit cell topology

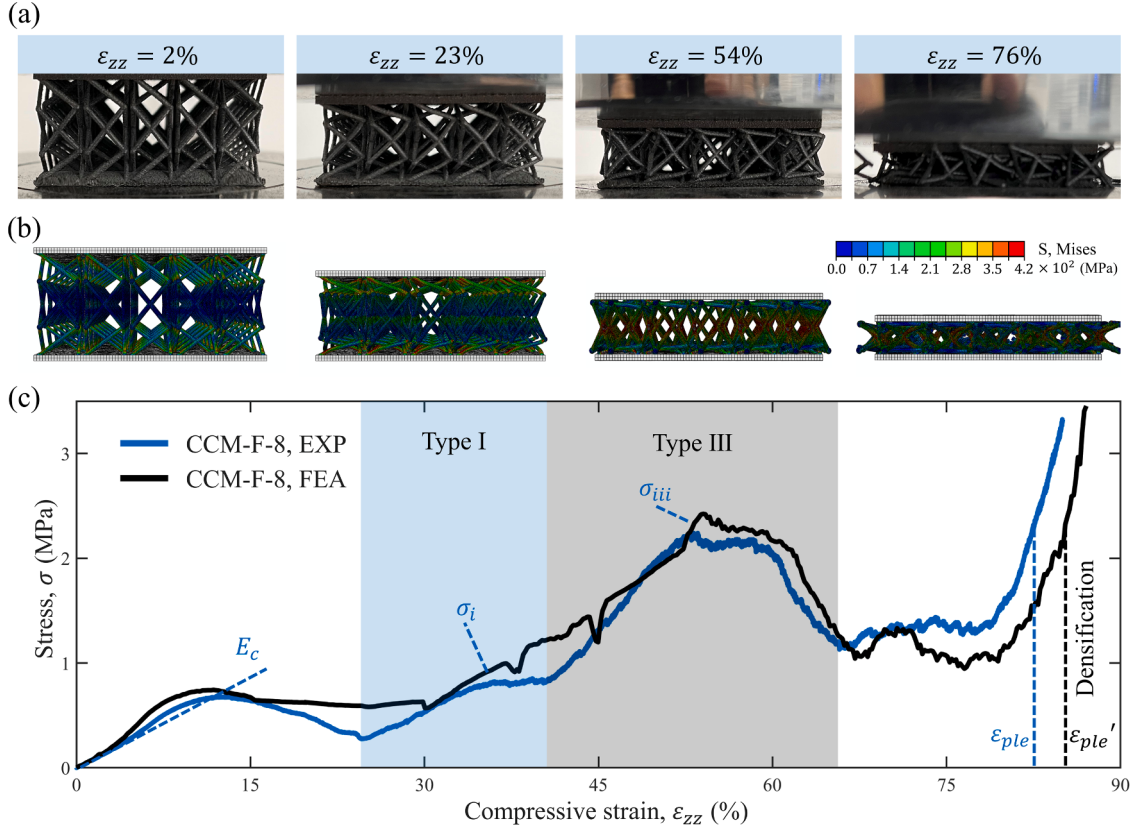


**Fig. 9.** The crushing behavior of CCM-F-8 sandwich structure. (a) In-situ observation of the compressive test at uniaxial strain  $\varepsilon_{zz} = 2\%$ ,  $23\%$ ,  $54\%$ , and  $76\%$  respectively (subfigures from the left to right), and (b) the corresponding FEA deformation history of the compressive procedure. (c) The experimental and numerical stress-strain curves of CCM-F-8. The sandwich sample was printed using SLM with  $5 \times 5 \times 1$  unit cells.

of NCM-T is typical in chiral mechanical metamaterials known as Z-shaped unit cell. And the response to compression is consistent with that of typical energy-absorbing materials as well – a low-stress plateau after yield until densification as shown in Fig. 6(c). Specifically, as the upper panel moved downward, the rods in the chiral part bent and drove the achiral part (a square frame in this case) to rotate through the joints, until these rods were flattened. During this process, the rods quickly entered the plastic stage and formed plastic hinges near the two ends of each rod, and fractures began to occur successively at these positions at  $\varepsilon_{pl} = 20\% \sim 25\%$ , causing the stress to drop from above 1 MPa to about half. This demonstrates that chiral metamaterial with Z-shaped topology itself is inherently flexible and has the advantage of absorbing energy in compression through bending and rotating, despite the brittle constituent materials. In contrast, as shown in Fig. 7, NCM-F-8 on the basis of NCM-T-8 presented an additional sudden increase in stress at  $\varepsilon_{pl} = 45\% \sim 65\%$ . This was resulted by the contact behavior between the achiral parts (the FCC lattice in this case) and the upper and lower panels, before which stage the chiral parts had been crushed and the stiffer FCC lattice borne the load instead. The results show that NCM-F absorbs more energy than NCM-T, but the corresponding SEA is reversed because of a higher density for the former kind of sandwich core layer.

Benefited from the contact between unit cells, CCM-F and CCM-T exhibited more complex mechanical behaviors and better performance in compression, as illustrated in Fig. 8 and Fig. 9. The enhancement of stiffness for CCM-F at  $\varepsilon_{pl} = 45\% \sim 65\%$  due to the contact between the achiral parts and the two panels is similar to that of NCM-F. More importantly, we can obtain the strengthening effect of intercellular contact on the compressive strength during the intermediate stage of plastic deformation ( $\varepsilon_{pl} = 20\% \sim 40\%$ ). To be specific, the achiral part of the unit cell prevents the other unit cells from rotating any further by

rod-to-rod contacts. Under this circumstance, the bending of the rods in the chiral part is hindered, thereby increasing the bearing capacity of the chiral metamaterial core gradually. It is noted that the failure mode of the rods remains unchanged which has been discussed in Section 3.1. Compared to CCM-T, CCM-F shows a hysteresis in the increase of stress on the curve due to intercellular contact and a smaller amplitude, which is determined by the characteristics of the chiral part defined by the geometrical parameters. And CCM-F has an additional contact behavior between the achiral part and the two panels. Overall, it is the CCM-F that has the higher EA and SEA, referring to Table 4.

Based on the above analysis, we summarized three types of contact modes before the CCM/NCM sandwich structure is completely crushed:

- i) Type I - Contact between the achiral parts of adjacent unit cells. This is a deliberately introduced contact situation by design. Such contact only occurs during the plastic deformation stage of the chiral parts of CCM sandwich structures, which is also the earliest among the three types of contact. Type I contact causes a higher stress response to compression until the chiral parts are crushed, and then the plastic deformation of the achiral parts begins.
- ii) Type II - Contact between the rod components within single chiral part. This is the most basic deformation mode of chiral metamaterials during compression, where the rods bend and rotate around the rotational center (center axis along z-axis of a unit cell) until they come into contact with each other. Plastic deformation is concentrated at the ends of the rods before contact. And after Type II contact, plastic deformation will continue with additional plastic hinges around the contact regions (see Appendix B for details). This type of contact occurs at the end of the chiral parts' compressive deformation prior to Type III contact (if

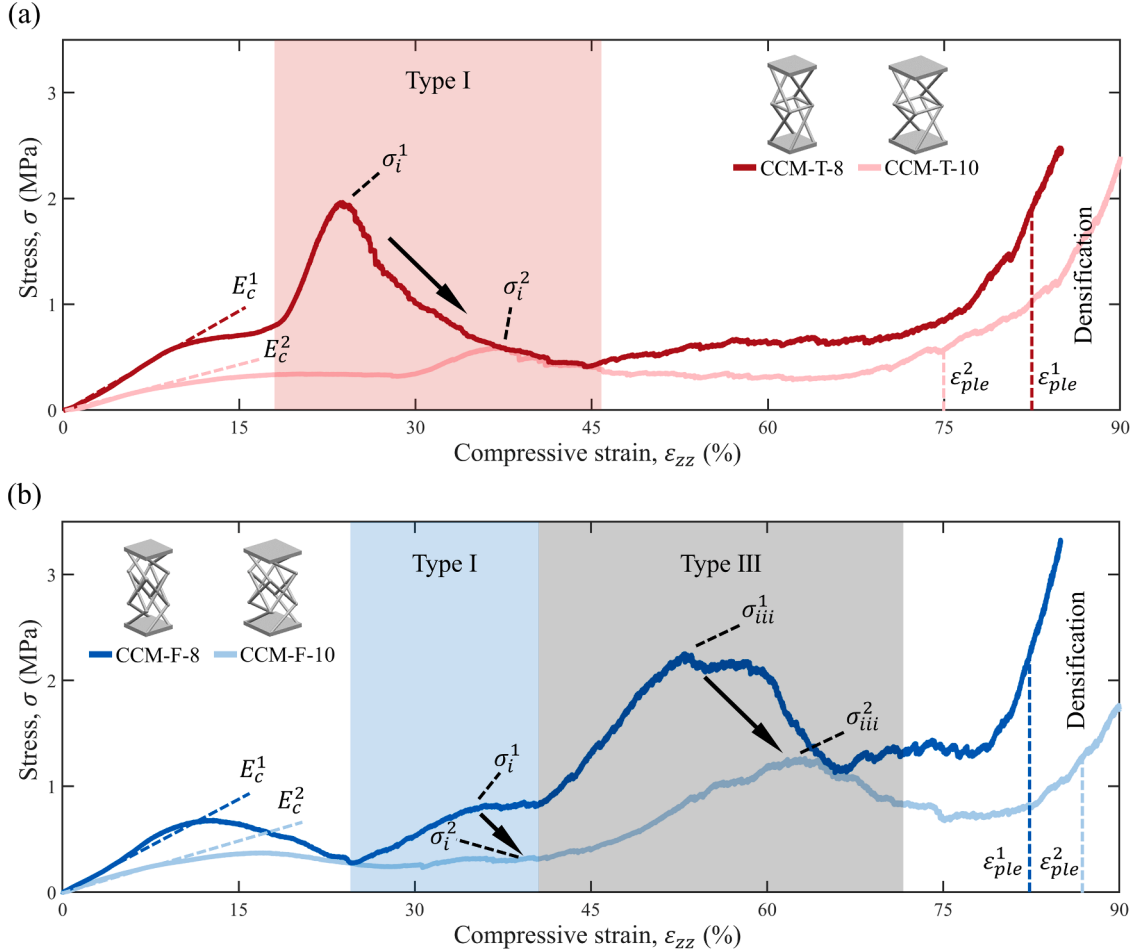


**Fig. 10.** The impact of the size of the chiral unit cell on the deformation pattern. (a) Comparison between CCM-T-8 and CCM-T-10. (b) Comparison between CCM-F-8 and CCM-F-10. The compressive performance indicators are superscripted with '1' for  $L_1 = 8\text{mm}$  and '2' for  $L_1 = 10\text{mm}$ .

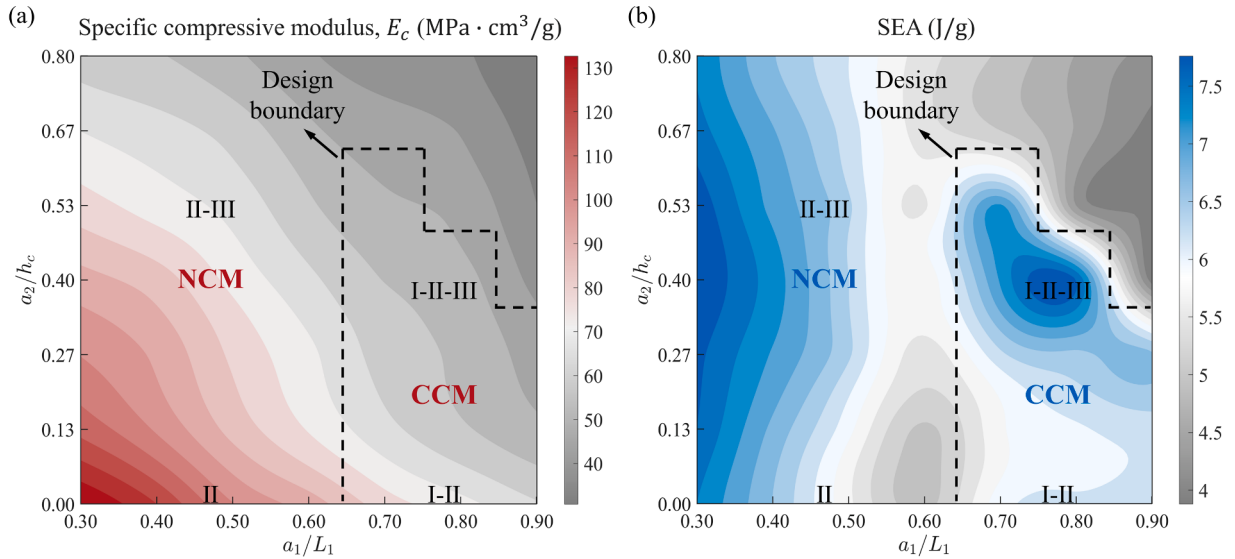


**Fig. 11.** The compressive performance distribution of sandwich structures in the design space. (a) The specific compressive modulus and (b) SEA of the chiral sandwich structures with respect to  $a_1/L_1$  and  $a_2/h_c$ . The results are derived by FEA with  $L_1 = 8\text{mm}$  and  $h_c = 18\text{mm}$ . The black dash lines represent the design boundary between CCM and NCM, along with different contact modes shown in the contours.

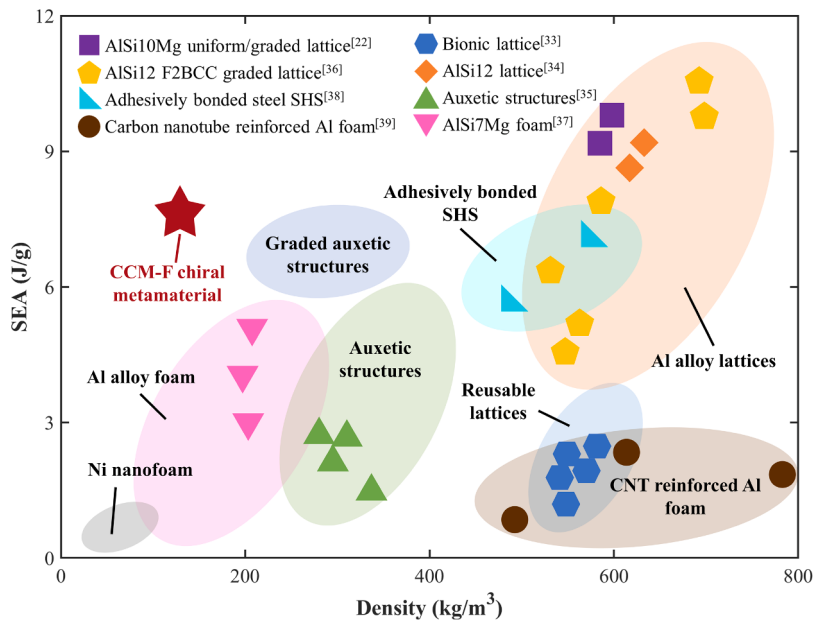


Fig. 12. The SEA Ashby diagram with respect to the density of light-weight materials. Representative categories of light-weight materials in recent research [33–39] are demonstrated including Al foam, Al lattices, spherical hollow structure (SHS), etc.

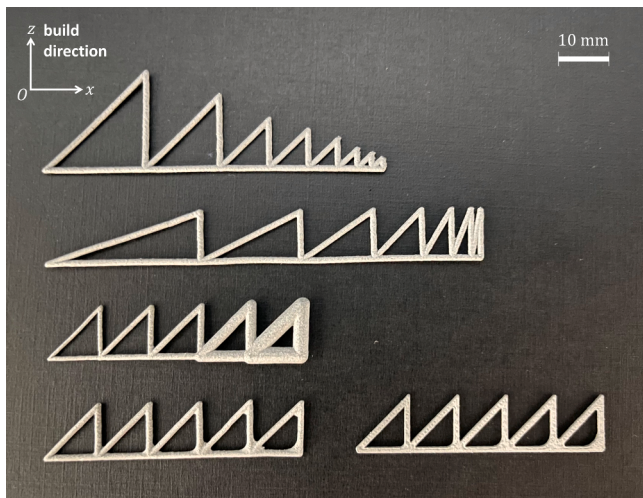


Fig. A1. The pre-test to examine the manufacturable rod diameter and inclination angle of SLM.

any), which also indicates the completion of energy absorption by these rod components.

- iii) Type III - Contact between the achiral part and the upper and lower panels. It happens in the middle to later stage of yield plateau where the chiral part has been crushed and the achiral part mainly bears the load until the whole core layer is densified. With stretch-dominated FCC type lattices as the achiral part, the stiffness of the chiral metamatte sandwich panel rapidly increases after Type III contact occurs.

With the combination of these contact modes, the strength of the sandwich structures changes with the compression. Type I contact increases the rigidity and compressive strength at around 20%~50% strain, while Type III contact causes a sudden increase in stress at around 50%~70% strain. The peak stress caused by these two contact modes are denoted as  $\sigma_i$  and  $\sigma_{iii}$  respectively in Fig. 7, Fig. 8, and Fig. 9. Moreover, the advantages of the metamatte with Type I contact on mechanical

responses and energy absorption are reflected in the higher elastic plateau and SEA, by comparing CCM-F-8 with NCM-F-8 (and CCM-T-8 with NCM-T-8). And by comparing the chiral sandwich structures with ( $a_2/h_c > 0$ , CCM-F-8 and NCM-F-8) and without FCC lattices ( $a_2/h_c = 0$ , CCM-T-8 and NCM-T-8), it implies that Type III contact also changes the strength of the core layer and enhances the total energy absorption. It should be pointed out that, given the geometrical parameters of the chiral unit cell, the SEA component improved by Type I contact is positively correlated with the number of boundaries where intercellular contact occurs, while the improvement by Type II and Type III contacts is proportional to the number of unit cells, denoted as

$$\text{SEA}_{\text{I}} \propto 2N(N-1), \quad \text{SEA}_{\text{II}} \propto N^2, \quad \text{SEA}_{\text{III}} \propto N^2 \quad (13)$$

where  $N = N_x = N_y$ . Obviously the effect from Type I contact is twice as much as that from either of the other two if  $N$  approaches infinite.

We further analyzed the influence of the size of the chiral unit cell by comparing CCM-F-8 and NCM-T-8 with CCM-F-10 and NCM-T-10. As shown in Fig. 10 and Table 4, the smaller the side length of the unit cell, the stronger the impact caused by Type I and Type III contacts, which means higher EA and compressive strength in amplitude. And these contact behaviors occur relatively later for larger  $L_1$  with  $d$  and  $h_c$  fixed. To explain this, the chiral part of the smaller unit cell has a higher length-to-width ratio and thus higher stiffness. Meanwhile, Type I contact has a strong boundary effect according to Eq. (13). That is, unlike the representative unit cell whose four sides all undergo Type I contact, the side faces on the boundary of the sandwich structure with free boundary condition are contact-free. Consequently, Type I contact is more sensitive to  $N$ .

Table 4 also demonstrated the contact modes of each category of CCM/NCM sandwich structure. Overall, the results embody a characteristic of multi-segment responses to static compression that is different from any traditional materials, i.e., the mechanical behavior of the material is non-uniform and artificially designed along the direction of the load, indicating a concept of functional gradient for load-bearing and energy absorption.

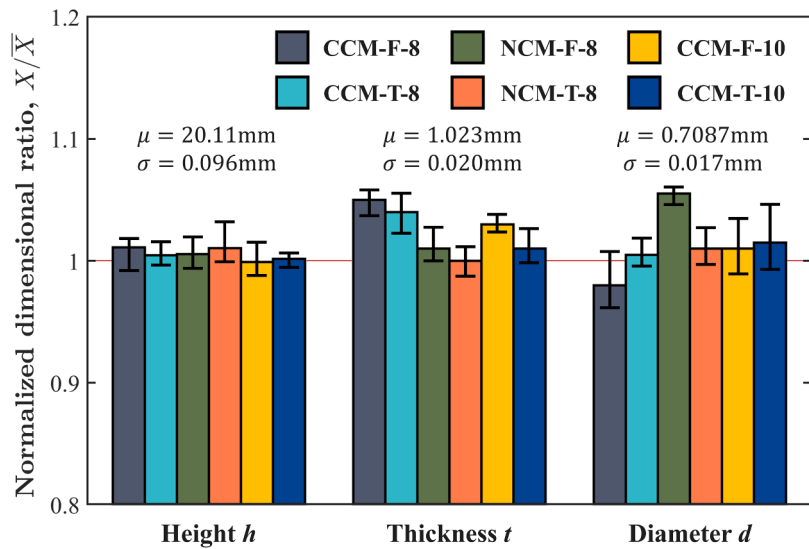


**Fig. A2.** The dimensional analysis of various categories of CCM/NCM sandwich structures.  $X/\bar{X}$  in y-axis represents the ratio of measured and the nominal sizes of overall height  $h$ , sheet thickness  $t$ , and rod diameter  $d$  respectively. The mean value  $\mu$  and the standard deviation  $\sigma$  are labelled above each bar group. And the respective maximum and minimum measurements are noted as the upper and lower edges.

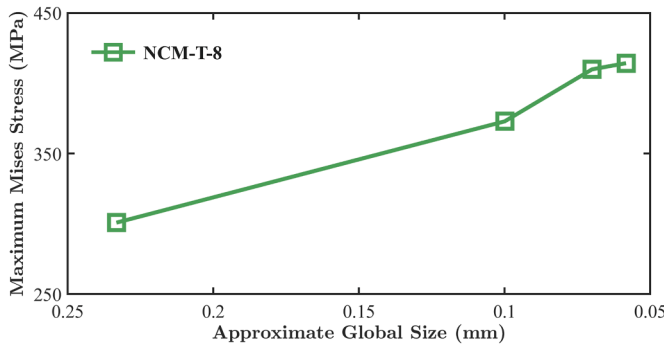


**Fig. A3.** The design of AlSi10Mg specimen and the conduct of tensile experiment. (a) The geometrical parameters of the tensile specimen. (b) The electrical universal testing machine Instron 5982 with DIC system.

**Table A1**  
Mechanical properties of AlSi10Mg.

Measurement	Condition	Metric
Young's modulus (GPa)	ASTM E8M	$67 \pm 7$
Ultimate strength (MPa)		$295 \pm 65$
Yield strength Rp0.2% (MPa)		$190 \pm 35$
Elongation at break (%)		$\geq 5$
Impact toughness (J)	ASTM E23	$31 \pm 1$

Values are based on average and expected spread of parts manufactured with standard parameters on a ProX DMP 320 (after stress relief).

### 3.3. Energy absorbing performance of CCM/NCM with respect to the design space

The energy absorption performance of the SLM chiral sandwich samples indicates that the additional rotation deformation contributes to the plastic stage of chiral core layer with complex contact modes that alters the strength during compression. Referring to the stress-strain curves, the energy absorption of the chiral metamaterials is mainly converted into internal energy through material deformation, which can be divided into:

- i) Elastic and plastic deformation dominated by the bending deformation of the rod components in the chiral parts;
- ii) Extrusion deformation and frictional dissipation of Type I contact after the compression-to-torsion rotation of the achiral parts;
- iii) Elastic and plastic deformation dominated by the axial deformation of the achiral parts after the failure of the chiral parts.

Results show that chiral metamaterials with I-II-III contact modes exhibit better energy-absorbing capacity than those with either I-II or I-III. Compared with I-II, I-II-III has a higher length-to-width ratio of the corresponding chiral parts, weakening the twisting ability and thus causes a hysteresis in Type II contact and a reduction in compressive strength of the corresponding plateau. However, the strength increment due to Type III contact is significant, so that the overall EA of the core layer with I-II-III is higher than that of I-II. And it should be noted that the relative density of I-II-III is relatively larger. Furthermore, compared with I-III, I-II-III has smaller compressive modulus but higher compressive strength on average, which reveals a mutual competition mechanism between Type II and III contacts.

With the deformation pattern and crushing mechanism derived, a further numerical investigation was carried out to estimate the energy absorption capability throughout the design space. As mentioned previously, with  $L_1$ ,  $d$ , and  $h_c$  fixed, the intercellular contact is mainly determined by the length and the height of the achiral part -  $a_1$  mainly determines Type I contact and  $a_2$  mainly determines Type III contact. Specifically, a larger  $a_1$  leads to earlier intercellular contact during deformation, and a smaller  $a_1$  results in later contact. And when it decreases to a certain level, the axial deformation responses of unit cells become independent of one another as a result of non-intercellular contact. When  $a_2$  is too large, i.e., close to 1, the structure may not meet the design requirements with a too small height of the chiral layer resulting in a small twist angle and no contact. Conversely, as  $a_2$  becomes 0, the structure simplifies to the normal Z-shaped topology. Herein, we constructed a parameter matrix composed by  $a_1/L_1$  varying from 0.3 to 0.9 and  $a_2/h_c$  varying from 0 to 0.8. The design boundary between CCM and NCM sandwich structures can be determined based on the criterion derived from Eq. (3) and Eq. (4). In this way, the distribution of SEA and specific compressive modulus of sandwich structures under compression were demonstrated as contours in Fig. 11.

Referring to Fig. 11(a), the stiffness of chiral metamaterials decreases as  $a_1/L_1$  or  $a_2/h_c$  increases, which represents the elastic response of

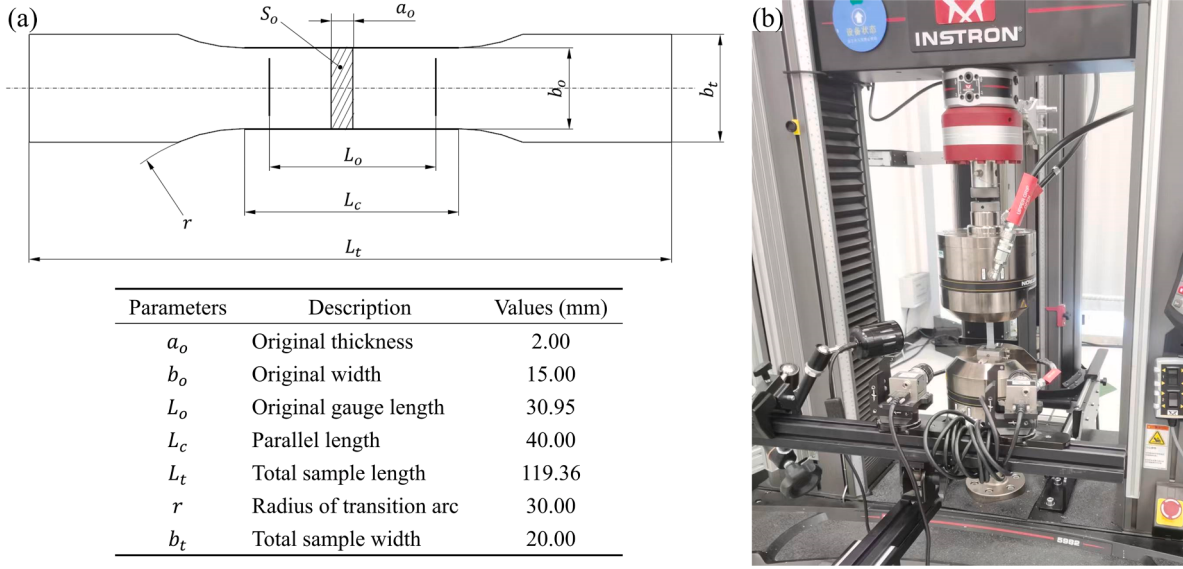


Fig. B1. The convergence analysis of element size. The maximum stress is extracted at  $\varepsilon_{zz} = 10\%$ .

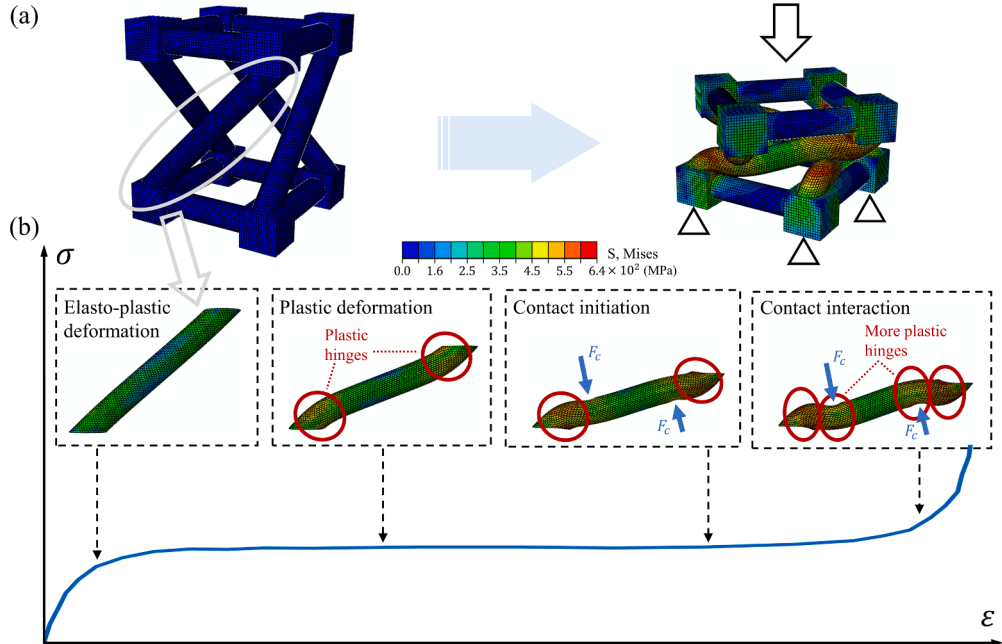


Fig. B2. The investigation on the compressive behavior of Z-shaped chiral unit cell. (a) The FEA model and the corresponding boundary conditions. (b) Analysis of the rod component of the unit cell under uniaxial compression based on the stress-strain curve, where different stages of deformation are demonstrated in the dash line squares.

materials before contact occurs. It has been illustrated that the Young's modulus of chiral metamaterial is lower than that of the achiral one in our previous study [18]. Herein, larger  $a_1$  and  $a_2$  make the lower elastic modulus in the initial phase of compression. The essence of this is that the greater the inclination of the diagonal rod (the angle between the rod axis and the positive direction of z-axis, which can be described as  $\gamma = f(\alpha, \beta)$ ), the greater the tangential component of the rod to the external uniaxial load. And it is more likely to deform in bending. It implies that chiral part transforms the force along z-axis into torsion in the xOy plane by reducing the stiffness and strength, resulting in greater plastic deformation. This "trade-off" leads to a proper application for chiral metamaterials to energy absorption where a mechanical response with low peak stress and long yield plateau is needed.

Moreover, the SEA variation with regard to the contact mode in Fig. 11(b) indicates that sandwich structure absorbs more energy with contact-aided twists. First of all, affected by  $a_1$  and  $a_2$ , the design domain of CCM is relatively more concentrated, with CCM-F performs better than CCM-T in SEA. It supports the above viewpoint on the energy absorption gain by I-II-III. Secondly, at small  $a_1$ , the SEA is also intuitively large due to the contribution of Type III contact by a slender achiral part. However, these NCM unit cell types are not effective in energy absorption theoretically because of the domination of stretching deformation over the bending deformation of the achiral part. And practically, the high length-to-width ratio of the achiral part can easily cause instability of the rod during compression. As a result, CCM-F turns out to be the most effective chiral metamaterial of the proposed designs in energy

absorbing.

Ultimately, to compare the presented CCM/NCM sandwich panels with the other structures and materials, the properties of many aluminum-based light-weight materials are illustrated through Ashby diagram. As shown in Fig. 12, the low density and good energy absorption performance of the proposed chiral metamaterials are highlighted.

#### 4. Conclusions

Chiral mechanical metamaterials exhibit advantages on energy absorption due to the unusual compression-to-rotation behavior. It converts the one-dimensional force to a 3D response, causing more plastic deformation. What's more, the contact between rod components of metamaterials increases the energy dissipation, which implies a potential in energy absorption improvement. Therefore, we proposed a category of chiral mechanical metamaterial with contact-aided twist, analysed the deformation mechanism under crush, explored the design space by parameterization, and derived the structure-property relationship of the material. Inspired by the lightweight nature and the complex deformation patterns of the chiral metamaterial, we applied it to the sandwich core layer and manufactured AlSi10Mg metal sandwich structures utilizing SLM. Through physical experiments and FEA modeling, we obtained the crushing behaviors of the proposed CCM/NCM sandwich structures which can be concluded as:

- i) The proposed sandwich panels can exhibit multi-segment mechanical responses to a flat compression, which is different from traditional materials or structures. It gives insights of how the combinations of bending-dominated and stretching-dominated lattices function as analogy to gradient materials.
- ii) The unique properties achieved by the microstructural design are less relevant to the choice of constituent material. Different from the brittleness characteristics of AlSi10Mg, the proposed CCM/NCM sandwich panels that constituted by AlSi10Mg exhibited a compressive behavior where the first plateau stress was not significant and the yield plateau stayed long, which signifies suitability for deformation energy absorption.
- iii) It shows that the three representative contact modes play important roles in tuning the elastic modulus, compressive strength, and corresponding energy absorption of crush. The chiral metamaterial with I-II-III mode performs the best in our

research. What's more, a mutual competition mechanism between Type II and III contacts is revealed, which provides guidance for the material design.

By the proposed mechanical metamaterials with contact-aided twist and the embodied design framework, the application of lightweight, high specific energy absorbing, and load-bearing structures is expected to be realised, e.g., multifunctional panels, impact-resistant shields, and cushioning layers. It should be noted that the nonlinear and dynamic responses of metal sandwich structures require further research considering the strain rate effects or multi-axes loads. In addition, the energy absorption and load-bearing performance of sandwich panels based on the chiral mechanical metamaterials can be further optimized by adjusting the topology, shape, size, and arrangement of unit cells. Future work of energy-absorbing chiral metamaterials includes gradient functional design [40,41], design and fabrication with much larger number of unit cells [17,42], computational-cost-mitigated optimization design method [43,44], etc.

#### CRediT authorship contribution statement

**Weiyun Xu:** Conceptualization, Methodology, Software, Writing – original draft. **Lei Zhang:** Writing – review & editing. **Boqin Zhang:** Visualization. **Hanyu Zhang:** Writing – review & editing. **Zhao Liu:** Data curation. **Ping Zhu:** Investigation, Supervision.

#### Declaration of Competing Interest

The authors declare that they have no known competing financial interests or personal relationships that could have appeared to influence the work reported in this paper.

#### Data availability

All data needed to evaluate the conclusions in the paper are present in the paper.

#### Acknowledgments

This work was sponsored by Natural Science Foundation of Shanghai (Grant No. 21ZR1431500 and No. 23ZR1431600).

## Appendix A

### A1. Dimensional analysis of the fabricated samples

Although we did not focus on the method of manufacturing process, a reliable 3D-printing fabrication quality of the chiral sandwich structures is an essential prerequisite for the later experimental validation in this paper. Hence, we firstly printed a batch of strut structures to examine the manufacturable rod diameter and inclination angle considering the self-support SLM technique, as shown in Fig. A1. The proper variation range of geometrical parameters was in this way pre-tested, within which the six types of CCM/NCM sandwich structures as in Table 2 were fabricated.

Next, the dimensional analysis was conducted to validate the forming accuracy in size and shape of the printed samples. We emphasized the analysis of the geometrical features along the build direction because the dimension in self-supported printing is more difficult to guarantee. Hereby we measured the overall height  $h$ , the sheet thickness  $t$ , and the strut diameter  $d$  of the fabricated samples. For each category of CCM/NCM sandwich structures, these measurements were averaged by three different locations, and divided by their respective nominal sizes for a fair comparison, as

$$\begin{aligned} \frac{1}{3} \sum h_i / \bar{h}, \\ \frac{1}{3} \sum t_i / \bar{t}, \\ \frac{1}{3} \sum d_i / \bar{d} \end{aligned} \quad (A1)$$

where  $\bar{h} = 20\text{mm}$ ,  $\bar{t} = 1\text{mm}$ , and  $\bar{d} = 0.7\text{mm}$ . As shown in Fig. A2, the relative errors are within  $\pm 5\%$ , and the respective mean and standard deviation were also derived. It shows a good agreement in geometry between the fabricated samples and the CAD models.

#### A2. Test of AlSi10Mg tensile specimens

Tensile specimens were fabricated and tested to obtain the mechanical properties of AlSi10Mg. The proportional specimens were designed according to ASTM E8M standard, as shown in Fig. A3. The experiment platform with DIC is presented as well.

As the constituent material of the proposed metamaterial, the specimens were stretched uniaxially to fracture to obtain its Young's modulus, yield strength and tensile strength. The tensile rate was  $0.04\text{mm/s}$ . The engineering stress and strain measured in experiment are transferred into true stress and strain. Next, in order to define the post-yield properties of the material for simulation, the logarithmic plastic strain is calculated as

$$\varepsilon_{LN}^{pl} = \varepsilon_t - \frac{\sigma_t}{E}, \quad (\text{A2})$$

where  $\sigma_t$  and  $\varepsilon_t$  are the true stress and the total true strain before the ultimate tensile stress point respectively, and  $E$  stands for the Young's modulus of AlSi10Mg. The mechanical properties are shown in Figure 4, along with the data provided by the manufacturer as listed in Table A1.

## Appendix B

### B1. Mesh convergence analysis of FEA

In order to confirm the appropriate mesh size of finite element models, we conducted the convergence analysis using the NCM-T-8 sandwich panel. The material properties, interaction, boundary condition, element types, and steps set up were the same as described in Section 2.3. Considering the geometrical features of the rod components, the element size was defined as  $d/3$ ,  $d/7$ ,  $d/10$ , and  $d/12$  respectively ( $d = 0.7\text{mm}$ ), and the maximum Von Mises stress at  $\varepsilon_{zz} = 10\%$  was extracted. As illustrated in Fig. B1, the predicted maximum stress had a relative error of  $1.06\%$  between  $d/10$  and  $d/12$ , implying a tendency of convergence. Thus, we chose an approximate global size of  $d/10 = 0.07\text{mm}$  to balance the accuracy and efficiency in FEA.

### B2. FEA of the plastic deformation of Z-shaped chiral unit cell

In order to investigate the deformation mechanism of chiral structure and the influence of the contact between rod components, the compression process of a Z-shaped chiral unit cell was simulated utilizing ABAQUS. Meshed by spatial continuum elements, the model was assigned the elastic and plastic properties of AlSi10Mg. The boundary condition of uniaxial compression was satisfied, where the bottom of the unit cell was fixed and the top was imposed a force along z-axis in the center.

Referring to Fig. B2, the compressive behavior of a Z-shaped unit cell ended with a stage of contact between the rod components, which we called Type I contact in this paper. By analysing the behavior of a single rod, the deformation under compression showed that it quickly entered the yield plateau after an elasto-plastic stage. The plastic hinges formed at the two ends of the rod where the local stress increased significantly. After the contact, the regions pressed by the contact forces gradually generated additional plastic hinges, which allowed the rod components to be fully deformed and increased the energy absorption of the unit cell.

## References

- [1] Akbari M, Mirabolghasemi A, Bolhassani M, Akbarzadeh A, Akbarzadeh M. Strut-based cellular to shellular funicular materials. *Adv Funct Mater* 2022;32:2109725. <https://doi.org/10.1002/adfm.202109725>.
- [2] Gao Z, Wang H, Sun H, Sun T, Wu Y, Leung CLA, Wang H. Additively manufactured high-energy-absorption metamaterials with artificially engineered distribution of bio-inspired hierarchical microstructures. *Composit Part B: Eng* 2022;247. <https://doi.org/10.1016/j.compositesb.2022.110345>.
- [3] Bauer J, Schroer A, Schwaiger R, Kraft O. Approaching theoretical strength in glassy carbon nanolattices. *Nat Mater* 2016;15:438–43. <https://doi.org/10.1038/nmat4561>.
- [4] Mukhopadhyay T, Adhikari S, Batou A. Frequency domain homogenization for the viscoelastic properties of spatially correlated quasi-periodic lattices. *Int J Mech Sci* 2019;150:784–806. <https://doi.org/10.1016/j.ijmecsci.2017.09.004>.
- [5] Zhao X, Wei L, Wen D, Zhu G, Yu Q, Ma ZD. Bending response and energy absorption of sandwich beams with novel auxetic honeycomb core. *Eng Struct* 2021;247:113204. <https://doi.org/10.1016/j.engstruct.2021.113204>.
- [6] Schumacher C, Bickel B, Rys J, Marschner S, Darao C, Gross M. Microstructures to control elasticity in 3D printing. *ACM Trans Graph* 2015;34:1–13. <https://doi.org/10.1145/2766926>.
- [7] Frenzel T, Findeisen C, Kadic M, Gumbsch P, Wegener M. Tailored buckling microlattices as reusable light-weight shock absorbers. *Adv Mater* 2016;28: 5865–70. <https://doi.org/10.1002/adma.201600610>.
- [8] Vangelatos Z, Gu GX, Grigoropoulos CP. Architected metamaterials with tailored 3D buckling mechanisms at the microscale. *Extreme Mech Lett* 2019;33:100580. <https://doi.org/10.1016/j.eml.2019.100580>.
- [9] Pham MS, Liu C, Todd I, Lerthanasarn J. Damage-tolerant architected materials inspired by crystal microstructure. *Nature* 2019;565:305–11. <https://doi.org/10.1038/s41586-018-0850-3>.
- [10] Fernandez-Corbaton I, et al. New twists of 3D chiral metamaterials. *Adv Mater* 2019;31:e1807742. <https://doi.org/10.1002/adma.201807742>.
- [11] Frenzel T, Kadic M, Wegener M. Three-dimensional mechanical metamaterials with a twist. *Science* 2017;358:1072–4. <https://doi.org/10.1126/science.aaq4640>.
- [12] Cui H, et al. Design and printing of proprioceptive three-dimensional architected robotic metamaterials. *Science* 2022;376:1287–93. <https://doi.org/10.1126/science.abn0090>.
- [13] Lipton JL, MacCurdy R, Manchester Z, Chin L, Cellucci D, Rus D. Handedness in shearing auxetics creates rigid and compliant structures. *Science* 2018;360:632–5. <https://doi.org/10.1126/science.aar4586>.
- [14] Frenzel T, Kopfler J, Jung E, Kadic M, Wegener M. Ultrasound experiments on acoustical activity in chiral mechanical metamaterials. *Nat Commun* 2019;10: 3384. <https://doi.org/10.1038/s41467-019-11366-8>.
- [15] Chen Y, Frenzel T, Guenneau S, Kadic M, Wegener M. Mapping acoustical activity in 3D chiral mechanical metamaterials onto micropolar continuum elasticity. *J Mech Phys Solids* 2020;137. <https://doi.org/10.1016/j.jmps.2020.103877>.
- [16] Ashby MF. The properties of foams and lattices. *Philosoph Transact Roy Soc A: Math Phys Eng Sci* 2006;364:15–30. <https://doi.org/10.1098/rsta.2005.1678>.
- [17] Frenzel T, et al. Large characteristic lengths in 3D chiral elastic metamaterials. *Commun Mater* 2021;2. <https://doi.org/10.1038/s43246-020-00107-w>.
- [18] Xu W, Liu Z, Wang L, Zhu P. 3D chiral metamaterial modular design with highly-tunable tension-twisting properties. *Mater Today Commun* 2022;30. <https://doi.org/10.1016/j.mtcomm.2021.103006>.
- [19] Meng L, et al. An emerging class of hyperbolic lattice exhibiting tunable elastic properties and impact absorption through chiral twisting. *Extreme Mech Lett* 2020; 40. <https://doi.org/10.1016/j.eml.2020.100869>.
- [20] Vangelatos Z, Micheletti A, Grigoropoulos CP, Fraternali F. Design and testing of bistable lattices with tensile architecture and nanoscale features fabricated by multiphoton lithography. *Nanomaterials* 2020;10:652. <https://doi.org/10.3390/nano10040652>.
- [21] Luo C, Han CZ, Zhang XY, Zhang XG, Ren X, Xie YM. Design, manufacturing and applications of auxetic tubular structures: a review. *Thin-Walled Structures* 2021; 163:107682. <https://doi.org/10.1016/j.tws.2021.107682>.
- [22] Maskery I, et al. A mechanical property evaluation of graded density Al-Si10-Mg lattice structures manufactured by selective laser melting. *Mater Sci Eng: A* 2016; 670:264–74. <https://doi.org/10.1016/j.msea.2016.06.013>.
- [23] Qi D, et al. Mechanical behaviors of SLM additive manufactured octet-truss and truncated-octahedron lattice structures with uniform and taper beams. *Int J Mech Sci* 2019;163:105091. <https://doi.org/10.1016/j.ijmecsci.2019.105091>.

- [24] Li M-Z, Stephani G, Kang K-J. New cellular metals with enhanced energy absorption: wire-Woven Bulk Kagome (WBK)-metal hollow sphere (MHS) hybrids. *Adv Eng Mater* 2011;13:33–7. <https://doi.org/10.1002/adem.201000165>.
- [25] Jovanova J, Nastevska A, Frecker M. Tailoring energy absorption with functional grading of a contact-aided compliant mechanism. *Smart Mater Struct* 2019;28. <https://doi.org/10.1088/1361-655X/ab281d>.
- [26] Coulais C, Sabbadini A, Vink F, van Hecke M. Multi-step self-guided pathways for shape-changing metamaterials. *Nature* 2018;561:512–5. <https://doi.org/10.1038/s41586-018-0541-0>.
- [27] Ha CS, Plesha ME, Lakes RS. Chiral three-dimensional isotropic lattices with negative Poisson's ratio. *Physica Status Solidi (b)* 2016;253:1243–51. <https://doi.org/10.1002/pssb.201600055>.
- [28] Li X, Yang Z, Lu Z. Design 3D metamaterials with compression-induced-twisting characteristics using shear-compression coupling effects. *Extrem Mech Lett* 2019;29. <https://doi.org/10.1002/j.eml.2019.100471>.
- [29] Berwind MF, Kamas A, Eberl C. A hierarchical programmable mechanical metamaterial unit cell showing metastable shape memory. *Adv Eng Mater* 2018;20: 1800771. <https://doi.org/10.1002/adem.201800771>.
- [30] Jenett B, Cameron C, Tourlomousis F, Rubio AP, Ochalek M, Gershenfeld N. Discretely assembled mechanical metamaterials. *Sci Adv* 2020;6. <https://doi.org/10.1126/sciadv.abc9943>.
- [31] Hooputra H, Gese H, Dell H, Werner H. A comprehensive failure model for crashworthiness simulation of aluminium extrusions. *Int J Crashworth* 2004;9: 449–64. <https://doi.org/10.1533/ijcr.2004.0289>.
- [32] Xiang YF, Wang M, Yu TX, Yang LM. Key performance indicators of tubes and foam-filled tubes used as energy absorbers. *Int J Appl Mech* 2015;7. <https://doi.org/10.1142/S175882511550060X>.
- [33] Sharma D, Hiremath SS. Bio-inspired repeatable lattice structures for energy absorption: experimental and finite element study. *Compos Struct* 2022;283: 115102. <https://doi.org/10.1016/j.compstruct.2021.115102>.
- [34] Ma Z, Zhang DZ, Liu F, Jiang J, Zhao M, Zhang T. Lattice structures of Cu-Cr-Zr copper alloy by selective laser melting: microstructures, mechanical properties and energy absorption. *Mater Des* 2020;187:108406. <https://doi.org/10.1016/j.matdes.2019.108406>.
- [35] Alomarah A, Masood SH, Sbarski I, Faisal B, Gao Z, Ruan D. Compressive properties of 3D printed auxetic structures: experimental and numerical studies. *Virtual Phys Prototyp* 2020;15:1–21. <https://doi.org/10.1080/17452759.2019.1644184>.
- [36] Al-Saeedi DSJ, Masood SH, Faizan-Ur-Rab M, Alomarah A, Ponnusamy P. Mechanical properties and energy absorption capability of functionally graded F2BCC lattice fabricated by SLM. *Mater Des* 2018;144:32–44. <https://doi.org/10.1016/j.matdes.2018.01.059>.
- [37] Jung A, Natter H, Diebel S, Lach E, Hempelmann R. Nanonickel coated aluminum foam for enhanced impact energy absorption. *Adv Eng Mater* 2011;13:23–8. <https://doi.org/10.1002/adem.201000190>.
- [38] Yiatis S, Marangos O, Votsis RA, Brennan FP. Compressive properties of granular foams of adhesively bonded steel hollow sphere blocks. *Mech Res Commun* 2018; 94:13–20. <https://doi.org/10.1016/j.mechrescom.2018.08.005>.
- [39] Aldoshan A, Khanina S. Effect of relative density on the dynamic compressive behavior of carbon nanotube reinforced aluminum foam. *Mater Sci Eng: A* 2017; 689:17–24. <https://doi.org/10.1016/j.msea.2017.01.100>.
- [40] Li S, et al. Sandwich panels with layered graded aluminum honeycomb cores under blast loading. *Compos Struct* 2017;173:242–54. <https://doi.org/10.1016/j.compositstruct.2017.04.037>.
- [41] Jiang H, Coomes A, Zhang Z, Ziegler H, Chen Y. Tailoring 3D printed graded architected polymer foams for enhanced energy absorption. *Composit Part B: Eng* 2021;224. <https://doi.org/10.1016/j.compositesb.2021.109183>.
- [42] Xu W, Wang L, Liu Z, Zhu P. General assembly rules for metamaterials with scalable twist effects. *Int J Mech Sci* 2023;108579. <https://doi.org/10.1016/j.ijmecsci.2023.108579>.
- [43] Vangelatos Z, et al. Strength through defects: a novel Bayesian approach for the optimization of architected materials. *Sci Adv* 2021;7. <https://doi.org/10.1126/sciadv.abk2218>.
- [44] Sheikhi HM. Systematic design of Cauchy symmetric structures through Bayesian optimization. *Int J Mech Sci* 2022;236:107741. <https://doi.org/10.1016/j.ijmecsci.2022.107741>.